The new two-image gravitational lens system CLASS B2319+051

D. Rusin, D.R. Marlow

Department of Physics and Astronomy, University of Pennsylvania, 209 S. 33rd St., Philadelphia, PA 19104-6396

M. Norbury, I.W.A. Browne, N. Jackson, P.N. Wilkinson

Jodrell Bank Observatory, University of Manchester, Macclesfield, Cheshire SK11 9DL, UK

C.D. Fassnacht, S.T. Myers

National Radio Astronomy Observatory, P.O. Box 0, Socorro, NM 87801

L.V.E. Koopmans[1], R.D. Blandford, T.J. Pearson, A.C.S. Readhead

California Institute of Technology, 105-24, Pasadena, CA 91125

A.G. de Bruyn[1]

Netherlands Foundation for Research in Astronomy, Postbus 2, NL-7990 AA Dwingeloo, Netherlands

ABSTRACT

We report the discovery of a new two-image gravitational lens system from the Cosmic Lens All-Sky Survey, CLASS B2319+051. Radio imaging with the Very Large Array (VLA) and Multi-Element Radio-Linked Interferometer Network (MERLIN) shows two compact components with a flux density ratio of $\simeq$ 5:1, separated by $1''\!.36$. Observations with the Very Long Baseline Array (VLBA) resolve each of the radio components into a pair of parity-reversed subcomponents. Hubble Space Telescope (HST) observations with the Near-Infrared Camera and Multi-Object Spectrometer (NICMOS) show a bright elliptical galaxy (G1) coincident with the radio position, and a second irregular galaxy (G2) $3''\!.4$ to the northwest. Previous spectroscopic studies have indicated that these galaxies are at different redshifts ($z_{G1} = 0.624$, $z_{G2} = 0.588$). Infrared counterparts to the lensed radio components are not detected in the NICMOS image, and the source redshift has not yet been determined. Preliminary mass modeling based on the VLBA subcomponent data indicates that the lensing potential includes a strong external shear contribution. A VLA monitoring program is currently being undertaken to measure the differential time delay.

Subject headings: cosmology: gravitational lensing

---

[1]and Kapteyn Astronomical Institute, Postbus 800, NL-9700 AV Groningen, Netherlands

1. Introduction

The Cosmic Lens All-Sky Survey (CLASS; Myers et al. 1995, 1999) seeks to discover new cases of gravitational lensing among flat-spectrum radio sources, and ultimately produce the largest and best studied sample of radio-selected lenses. CLASS builds upon the success of the Jodrell-VLA Astrometric Survey (JVAS; Patnaik et al. 1992; Browne et al. 1998; Wilkinson et al. 1998; King et al. 1999) and extends the search to weaker flux densities. The gravitational lens systems discovered by JVAS and CLASS are powerful tools for investigating a wide range of astrophysical and cosmological problems. First, arcsecond-scale lenses directly probe the inner several kiloparsecs of galaxies at intermediate redshift (Kochanek 1991), and can place vital constraints on their mass distributions. These studies indicate that the mass profiles of early-type lensing galaxies are close to isothermal (e.g., Kochanek et al. 1995; Cohn et al. 2001; Rusin & Ma 2001). Second, measured time delays between the images of a lensed source, when combined with a well-constrained mass model, allow for a determination of the Hubble constant (Refsdal 1964). Thus far time delays have been measured for seven gravitational lens systems (Schechter et al. 1997; Kundic et al. 1997; Lovell et al. 1998; Wisotzki et al. 1998; Biggs et al. 1999; Fassnacht et al. 1999b; Koopmans et al. 2000) and favor a Hubble constant of $H_0 = 74 \pm 8\,\mathrm{km\,s^{-1}\,Mpc^{-1}}$, assuming a flat cosmological model with $\Omega_\Lambda = 0.7$ (Koopmans & Fassnacht 1999). Third, the lensing rate in a systematic survey can place upper limits on the cosmological constant (Turner, Ostriker & Gott 1984; Turner 1990). Recent analyses favor $\Omega_\Lambda \leq 0.65$ for flat cosmologies (Kochanek 1996; Falco, Kochanek & Muñoz 1998; Quast & Helbig 1999).

Sources in the first two phases of CLASS were selected from the 87GB 5 GHz catalog (Gregory & Condon 1991), with $S_5 \geq 25$ mJy and spectral index $\alpha \geq -0.5$ (where $S_\nu \propto \nu^\alpha$) between 5 GHz and the 327 MHz Westerbork Northern Sky Survey (WENSS; Rengelink et al. 1997) or the 365 MHz Texas Survey (Douglas et al. 1996). Recently, the sources in the CLASS sample were reselected using the 5 GHz GB6 catalog (Gregory et al. 1996) and the 1.4 GHz NRAO VLA Sky Survey (NVSS; Condon et al. 1998), with a 5 GHz cutoff of 30 mJy and spectral index $\alpha \geq -0.5$ between 1.4 and 5 GHz. Spectral selection helps make CLASS a powerful and efficient lens survey. The flat-spectrum CLASS sample is dominated by sources with intrinsically compact morphologies, which eases the identification of lenses and simplifies calculations of the statistical lensing rate. Furthermore, compact sources tend to be variable, thereby making possible the measurement of time delays from the lightcurves of lensed images.

The CLASS sample was observed using the Very Large Array (VLA) in A configuration at 8.4 GHz, which offers a resolution of $\simeq 250$ mas. Observations of 3C286 were used to set the flux density scale. The VLA data were calibrated in the Astronomical Image Processing System (AIPS), and mapped using an automated script within the imaging package DIFMAP (Shepherd 1997). The data were then modeled with Gaussian components, which provides a quantitative description of the observed radio morphology. Sources modeled with multiple compact components are selected as preliminary lens candidates. These candidates are followed up with high resolution radio observations using the Multi-Element Radio-Linked Interferometer Network (MERLIN; res-

olution of $\simeq$ 50 mas at 5 GHz), and then the Very Long Baseline Array (VLBA; resolution of $\simeq$ 5 mas at 5 GHz) for the few surviving sources. The vast majority of the lens candidates are rejected on surface brightness and morphological grounds, and are instead shown to be core-jet sources. Candidates survive the radio filter if their components have compact or correlated structure at the milliarcsecond scale. These are then followed up further with optical and/or near-infrared imaging and spectroscopy.

CLASS survey observations of over 13000 sources were conducted in four phases (CLASS 1–4) from spring 1994 to summer 1999, and are now complete. The first phase of CLASS observations (CLASS–1) has yielded five new lens systems: B0128+437 (Phillips et al. 2000), B0712+472 (Jackson et al. 1998), B1600+434 (Jackson et al. 1995), B1608+656 (Myers et al. 1995) and B1933+503 (Sykes et al. 1998). The second series of observations (CLASS–2) has produced another five lenses: B0739+366 (Marlow et al. 2001), B1127+385 (Koopmans et al. 1999), B1555+375 (Marlow et al. 1999b), B2045+265 (Fassnacht et al. 1999a), and the one presented in this paper, B2319+051. Two additional lens systems have recently been discovered during the third phase of CLASS observations (CLASS–3): B1152+199 and B1359+154 (Myers et al. 1999; Rusin et al. 2000). Radio follow-up observations of the remaining CLASS–3 and CLASS–4 candidates are nearly complete.

Here we report the discovery of a new two-image gravitational lens from CLASS–2: B2319+051. In section 2 we describe radio observations of the system with the VLA, MERLIN and VLBA. Section 3 presents near-infrared imaging with the Hubble Space Telescope. Preliminary mass modeling of B2319+051 is described in Section 4. Section 5 summarizes our results and discusses future work.

2. Radio Observations

B2319+051 was observed on 1995 August 13 during the second phase of the CLASS survey observations. The 8.4 GHz discovery snapshot map has an rms noise of 330 μJy/beam and is displayed in Fig. 1. The source consists of two compact components with flux densities of 27.4 ± 0.3 mJy (A) and 5.0 ± 0.3 mJy (B) in a north-south orientation, separated by $1''\!\!.36$. Follow-up VLA 1.4, 5, 8.4 and 15 GHz A configuration observations were performed on 1999 July 29 to investigate the spectral properties of the radio components. The flux density scale was set by observations of the calibrator source J2355+498. The VLA data sets were calibrated in AIPS using the standard procedure and analyzed in DIFMAP. In each case the visibility data were fit to a pair of compact Gaussian components using several iterations of model-fitting and phase-only self-calibration (solution interval of 0.5 min). The component flux densities are given in Table 1, and the radio spectra are plotted in Fig. 2. The radio spectra exhibit striking similarity, with overall spectral indices between 1.4 and 15 GHz of $\alpha_{1.4}^{15} = -0.66 \pm 0.01$ (A) and $\alpha_{1.4}^{15} = -0.61 \pm 0.05$ (B), respectively. This argues against the identification of A and B as either two independent quasars or components of a core-jet structure. However, nearly identical radio spectra would be expected for images of a gravitationally lensed source.

MERLIN 5 GHz observations of B2319+051 were performed on 1996 December 26 for a total integration time of 1 hr, and again on 1998 February 24 for 8.5 hr to improve the surface brightness sensitivity. Observations of 3C286 were used to set the flux density scale. The data were calibrated in AIPS and imaged in DIFMAP by repeating a cycle of cleaning and phase-only self-calibration, starting with long solution intervals (40 min) and gradually decreasing to a minimum interval of 2 min. Once the model had sufficiently converged, an amplitude self-calibration was performed using a solution interval of 30 min. The final map has an rms noise of 70 μJy/beam and is shown in Fig 3. The data were modeled by two compact Gaussian components with flux densities of 44.0 ± 0.1 mJy (A) and 8.8 ± 0.1 mJy (B). No further emission was detected down to the 3σ level of the maps. The compactness of each radio component in the MERLIN map offers further evidence for the lensing hypothesis.

VLBA 5 GHz observations of B2319+051 were performed on 1997 August 3. The observations were obtained using five separate snapshots, each of seven minutes duration, over a range of hour angles to synthesize uv coverage. The system was reobserved at 5 GHz on 2000 September 18 for 11 hr to improve the sensitivity. In each case, phase referencing was implemented using the nearby calibrator source J2320+052. Fringe fitting was performed on J2320+052 and the solutions were transferred directly to B2319+051. The calibrated data were then imaged in DIFMAP using several iterations of cleaning and phase-only self-calibration, with a solution interval of 5 min. Maps from the deep observation are presented in Fig. 4 and have an rms noise of 50 μJy/beam. Each of the radio components is resolved into a pair of compact subcomponents (A1 and A2, B1 and B2), indicative of a "core-knot" source morphology. In addition, we identify a very weak emission feature (A3) as the beginning of a radio jet connecting A1 and A2. A corresponding feature is not obvious in B, but its detection is greatly hindered by the decreased flux density and angular size of the component. B1 does however appear to be slightly extended along the east-west direction, possibly signaling the presence of this emission feature. While the maps we present employ natural visibility weighting, the higher resolution obtained by switching to uniform weighting is more than offset by the decreased sensitivity, and did not improve the analysis. The visibility data were well fit by a total of five compact (< 1 mas) Gaussian components, using iterated cycles of model-fitting and phase-only self-calibration. The positions and flux densities of the subcomponents are listed in Table 2.

Deep 1.7 GHz VLBA observations of B2319+051 were obtained on 1999 August 12. The total integration time was 12 hr. Phase referencing and fringe fitting were performed with the nearby JVAS source J2322+082. The calibration and imaging procedures were identical to those described above. The resulting maps have an rms noise of 55 μJy/beam and are displayed in Fig. 5. The substructure observed in the 1.7 GHz maps matches that detected at 5 GHz. The data were modeled by five Gaussian components that closely correspond to those derived from the 5 GHz observations. Table 2 lists the flux densities of these components. The residual map was searched for evidence of faint compact emission features that could be associated with a third "odd" image of the source (Rusin & Ma 2001), but none were found down to the detection threshold.

The milliarcsecond-scale substructure of the B2319+051 radio components contains the un-mistakable signature of gravitational lensing. First, components A and B share nearly identical morphologies, as would be expected for images of a common background source. Second, the rel-ative inversion of the radio components is a textbook example of lensing-induced parity reversal (e.g., Schneider, Ehlers & Falco 1992). Third, the brighter component (A) covers a larger angular size, consistent with the conservation of surface brightness by gravitational lensing. Taken together, these observations offer compelling evidence that B2319+051 is a gravitational lens system.

Finally, we searched for changes in the substructure of the B2319+051 radio images by compar-ing the relative positions of the core and knot subcomponents in the 1997 and 2000 VLBA 5 GHz data. The likelihood of detecting evolving superluminal jets is expected to be enhanced for lensed radio sources, as magnification would increase the apparent transverse velocity. Jet evolution may offer useful constraints on the mass model, and in particular on the local magnification matrices, but this effect has not yet been observed in any gravitational lens system. We find that the A1–A2 and B1–B2 separations in the 1997 and 2000 data sets are each consistent to within 0.1 mas. Our tests indicate that this is close to the reliability limit of DIFMAP model-fitting. Consequently, there is no evidence for evolving radio substructure in B2319+051 at this time.

3.   HST Imaging and Astrometry

Hubble Space Telescope (HST) observations of B2319+051 were obtained on 1998 May 30 with the Near-Infrared Camera and Multi-Object Spectrometer (NICMOS). The F160W filter was used, which is centered at 1.6μm and corresponds roughly to ground-based H band. The observations made use of the NIC2 camera, with a detector scale of 75 mas/pixel and a field-of-view of $19''.2 \times 19''.2$. The total exposure time was 2624 sec. The data were subjected to the standard NICMOS calibration pipeline, involving bias and dark current subtraction, flat-field correction, cosmic ray removal and photometric calibration. The final image is displayed in Fig. 6a. A bright elliptical galaxy (G1) is observed at the position of the radio system, but no counterparts to the radio images are detected. This suggests a very optically-faint lensed source, similar to B1127+385 (Koopmans et al. 1999) or B1933+503 (Marlow et al. 1999a). The observation of a galaxy close to the expected position does, however, satisfy an important criterion of the lensing hypothesis. A second, irregular galaxy (G2) lies $3''.4$ to the northwest of G1. A contour plot of the NICMOS image (Fig. 6b) clearly shows that G2 is composed of two subcomponents (G2a and G2b).

Photometry and relative astrometry were performed on G1 and G2 (Table 3). The elliptical surface brightness profile of G1 has an axis ratio of 0.63 ± 0.02 (at the outmost isophote) and a position angle of $52° \pm 5°$. The integrated F160W magnitudes are 18.2 and 19.1 for G1 and G2, respectively, with an uncertainty of ±0.15. Recent spectroscopic observations using the Low Resolution Imaging Spectrograph (LRIS) on the W. M. Keck telescope have demonstrated that the galaxies are not physically associated: $z_{G1} = 0.624$ and $z_{G2} = 0.588$ (Lubin et al. 2000). The spectrum of G1 is consistent with an early-type galaxy. G1 has approximately the luminosity of

an E/S0 $L*$ galaxy, including a K-correction but no evolutionary correction (Poggianti 1997). The spectrum of G2 shows strong Balmer absorption lines which, when combined with the irregular morphology, suggest an interacting or merging system.

The absence of detectable counterparts to the lensed radio components means that we cannot determine the positions of the galaxies relative to the images using any one data set. We therefore attempted to extract the absolute coordinates of G1 from the Keck observations of Lubin et al. (2000). Reference stars were selected from the USNO A2.0 Catalog (Monet et al. 1996) and the astrometric solutions were calculated using Judy Cohen's `coordinates` program, which takes into account the distortions introduced by the LRIS optics. Eight unsaturated reference stars were selected for the program, and the estimated final rms position error is $0\rlap{.}''45$. Unfortunately, the saturation of many reference stars in the Keck image makes sub-pixel accuracy impossible with the current data set. With the solutions from the `coordinates` program, we have determined the position of G1 to be RA 23 21 40.817 Dec +05 27 36.57 (J2000). Based on the VLBA positions of the lensed radio components, this would place G1 at $(0\rlap{.}''27, -0\rlap{.}''66)$ relative to A1, roughly between the two lensed images.

4. Mass Modeling

B2319+051 presents a greater modeling challenge than many two-image gravitational lens systems due to the lack of detected optical/infrared counterparts to the lensed radio components. Though the astrometry is not adequate to robustly fix the position of the lensing galaxy at this time, the milliarcsecond-scale radio substructure offers a sufficient number of constraints to test simple mass models. In this analysis we use the eight coordinates (x, y) of A1, A2, B1 and B2, as well as the two 5 GHz flux density ratios $r_1 = |S_{B1}/S_{A1}|$ and $r_2 = |S_{B2}/S_{A2}|$. Modeling was performed with an image plane minimization (Kochanek 1991), which optimized the fit statistic

$$\chi^2 = \sum_{i=A1,A2,B1,B2} \left[\frac{(x_i' - x_i)^2}{\Delta x_i^2} + \frac{(y_i' - y_i)^2}{\Delta y_i^2} \right] + \sum_{i=1,2} \frac{(r_i' - r_i)^2}{\Delta r_i^2} \tag{1}$$

where primed quantities are model-predicted and unprimed quantities are observed. We assumed a tolerance of $\Delta x = \Delta y = 0.1$ mas on the image positions and 5% on each of the flux densities ($\Delta r \simeq 7\%$) to account for possible modeling errors and source variability. A flat $\Omega_\Lambda = 0.7$ universe with $H_0 = 100h \, \mathrm{km \, s^{-1} \, Mpc^{-1}}$ and a source redshift of $z = 1.5$ were assumed for all calculations.

We first modeled B2319+051 using a singular isothermal ellipsoid mass distribution (SIE; Kormann, Schneider & Bartelmann 1994) with surface density

$$\Sigma(x, y) = \frac{\sigma^2}{2G} \frac{\sqrt{f}}{\sqrt{x^2 + f^2 y^2}} \tag{2}$$

where σ is the line-of-sight velocity dispersion and f is the projected axial ratio. Including the four parameters required to describe the unlensed source subcomponents, the model has nine free

parameters. Consequently, the number of degrees of freedom (NDF) is one. Not only does the model offer a rather poor fit to the radio data ($\chi^2/\mathrm{NDF} = 3.1$), but the mass distribution is predicted to lie at a position angle of $\simeq -30°$, nearly orthogonal to that of the observed surface brightness of G1. This is unlikely to be a consistent scenario, as modeling studies have demonstrated that lensing mass distributions are typically well aligned with the light (Keeton, Kochanek & Falco 1998). Fixing the mass distribution at the observed galaxy position angle of $52°$ leads to an unacceptable fit. Even when the coordinate uncertainties are relaxed to a very liberal 1 mas, $\chi^2/\mathrm{NDF} = 14$ for $\mathrm{NDF} = 2$, with mismatch of the subcomponent positions dominating the fit statistic. We interpret the poor performance of the single galaxy model as evidence that external shear is significantly influencing the lensing potential. Because the SIE model requires an ellipticity oriented at $\simeq -30°$, galaxies along this axis are likely to be responsible for the shear. Lubin et al. (2000) detect several galaxies, including G2, to the northwest of the system. These are likely candidates for the perturbing mass.

We therefore expanded the lens model to include an external shear field of constant direction and magnitude. To reduce the number of free parameters and ensure a constrained model, we set the position angle and axial ratio of the SIE to the observed values of the G1 surface brightness. The SIE + shear model provides a much improved fit to the radio data ($\chi^2/\mathrm{NDF} = 0.45$ with $\mathrm{NDF} = 1$). The optimized model parameters are listed in Table 4. The preferred shear field has a magnitude of $\gamma = 0.14$ and a position angle of $-22°$. G2 is unlikely to account for all of the model-predicted shear, unless it has a much higher mass-to-light ratio than G1. (An isothermal mass distribution at $3''\!\!.4$ requires a velocity dispersion of $\simeq 260\,\mathrm{km\,s^{-1}}$ to produce a shear field with $\gamma = 0.14$.) The position of the lensing galaxy ($0''\!\!.21$, $-0''\!\!.79$) agrees well with that derived from our LRIS astrometry. The predicted time delay between components A and B is $\simeq 18h^{-1}$ days for a flat $\Omega_\Lambda = 0.7$ cosmology.

5. Summary and Future Work

VLA and MERLIN observations of CLASS B2319+051 show two compact radio components separated by $1''\!\!.36$. Both components have virtually identical radio spectra between 1.4 and 15 GHz, consistent with them being images of a single background source. VLBA 5 GHz observations resolve each of the components into a pair of compact subcomponents. VLBA 1.7 GHz observations confirm this finding. The similar morphologies, consistent angular sizes and relative inversion of the radio components provide powerful evidence in support of the lensing hypothesis. HST/NICMOS imaging has revealed a bright elliptical galaxy at the expected position, along with a second irregular galaxy $3''\!\!.4$ to the northwest. Infrared counterparts to the radio components were not detected in this observation. However, the radio spectra and substructure along with the identification of a lensing galaxy argue that B2319+051 is, indeed, a genuine gravitational lens system.

Preliminary mass modeling has demonstrated that an isolated galaxy is unable to account for the VLBA substructure while remaining consistent with the properties of the lensing galaxy G1. Because an isolated SIE is required to be oriented nearly perpendicular to the observed surface

brightness of G1, nearby galaxies may be contributing significant ellipticity to the lensing potential. The introduction of external shear allows for an excellent fit to the data, even when the position angle and axial ratio of the SIE are fixed to match the G1 surface brightness. The favored shear direction is consistent with mass distributions located to the northwest of G1, as detected by Lubin et al. (2000). Considering our inability to robustly fix the position of the primary lensing mass relative to the lensed images, it is quite remarkable that the simple substructure in the B2319+051 radio components not only strongly excludes an isolated galaxy model, but also selects a reasonable direction for the external shear field.

Of paramount importance to future studies of B2319+051 is the detection of optical/infrared counterparts to the lensed images. The positions of these images relative to the lensing galaxy will provide an essential check for our preliminary modeling attempt, while offering additional constraints for the construction of more realistic mass models. The detection of these images would also be a first step toward measuring the source redshift, which is a vital ingredient for Hubble constant determination. B2319+051 is currently being monitored as part of a large VLA program to measure time delays in JVAS/CLASS gravitational lens systems.

REFERENCES

Biggs, A.D., Browne, I.W.A., Helbig, P., Koopmans, L.V.E., Wilkinson, P.N., & Perley, R.A. 1999, MNRAS, 304, 349

Browne, I.W.A., Wilkinson, P.N., Patnaik, A.R., & Wrobel, J.M. 1998, MNRAS, 293, 257

Cohn, J.D., Kochanek, C.S., McLeod, B.A., & Keeton, C.R. 2001, ApJ, in press (astro-ph/0008390)

Condon, J.J., Cotton, W.D., Greisen, E.W., Yin, Q.F., Perley, R.A., Taylor, G.B., & Broderick, J.J. 1998, AJ, 115, 1693

Douglas, J.N., Bash, F.N., Bozyan, F.A., Torrence, G.W., & Wolfe, C. 1996, AJ, 111, 1945

Falco, E.E., Kochanek, C.S., & Muñoz, J.A. 1998, ApJ, 494, 47

Fassnacht, C.D., et al. 1999a, AJ, 117, 658

Fassnacht, C.D., Pearson, T.J., Readhead, A.C.S., Browne, I.W.A., Koopmans, L.V.E., Myers, S.T., & Wilkinson, P.N. 1999b, ApJ, 527, 498

Gregory, P.C., & Condon, J.J. 1991, ApJS, 75, 1011

Gregory, P.C., Scott, W.K., Douglas, K., & Condon, J.J. 1996, ApJS, 103, 427

Jackson, N., et al. 1995, MNRAS, 274L, 25

Jackson, N., et al. 1998, MNRAS, 296, 483

Keeton, C.R., Kochanek, C.S., & Falco, E.E. 1998, ApJ, 509, 561

King, L.J., Browne, I.W.A., Marlow, D.R., Patnaik, A.R., & Wilkinson, P.N. 1999, MNRAS, 307, 225

Kochanek, C.S. 1991, ApJ, 373, 354

Kochanek, C.S. 1995, ApJ, 445, 559

Kochanek, C.S. 1996, ApJ, 466, 638

Koopmans, L.V.E., et al. 1999, MNRAS, 303, 727

Koopmans, L.V.E., & Fassnacht, C.D. 1999, ApJ, 527, 513

Koopmans, L.V.E., de Bruyn, A.G., Xanthopoulos, E., & Fassnacht, C.D. 2000, A&A, 356, 391

Kormann, R., Schneider, P., & Bartelmann, M. 1994, A&A, 284, 285

Kundic, T., et al. 1997, ApJ, 482, 75

Lovell, J.E.J., Jauncey, D.L., Reynolds, J.E., Wieringa, M.H., King, E.A., Tzioumis, A.K., McCullough, P.M., & Edwards, P.G. 1998, ApJ, 508L, 51

Lubin, L.M., Fassnacht, C.D., Readhead, A.C.S., Blandford, R.D., & Kundic, T. 2000, AJ, 119, 451

Marlow, D.R., Browne, I.W.A., Jackson, N., & Wilkinson, P.N. 1999a, MNRAS, 305, 15

Marlow, D.R., et al. 1999b, AJ, 118, 654

Marlow, D.R., et al. 2001, AJ, 121, 619

Monet, D., et al. 1996, USNO-SA2.0 (U.S. Naval Observatory, Washington DC)

Myers, S.T., et al. 1995, ApJ, 447L, 5

Myers, S.T., et al. 1999, AJ, 117, 2565

Patnaik, A.R., Browne, I.W.A., Wilkinson, P.N., & Wrobel, J.M. 1992, MNRAS, 254, 655

Phillips, P.M., et al. 2000, MNRAS, 319L, 7

Poggianti, B.M. 1997, A&AS, 122, 399

Quast, R., & Helbig, P. 1999, A&A, 344, 721

Refsdal, S. 1964, MNRAS, 128, 307

Rengelink, R.B., Tang, Y., de Bruyn, A.G., Miley, G.K., Bremer, M.N., Roettgering, H.J.A., & Bremer, M.A.R. 1997, A&AS, 124, 259

Rusin, D., Hall, P.B., Nichol, R.C., Marlow, D.R., Richards, A.M.S., & Myers, S.T. 2000, ApJ 533L, 89

Rusin, D., & Ma, C.-P. 2001, ApJ, 549L, 33

Schechter, P.L., et al. 1997, ApJ, 475L, 85

Schneider, P., Ehlers, J., & Falco, E.E. 1992, *Gravitational Lenses* (Berlin: Springer-Verlag)

Shepherd, M.C. 1997, in Astronomical Data Analysis Software and Systems IV, eds. G. Hunt & H. E. Payne, (ASP Conference Series, v125) 77

Sykes, C.M., et al. 1998, MNRAS, 301, 310

Turner, E.L., Ostriker, J.P., & Gott, J.R. 1984, ApJ, 284, 1

Turner, E.L. 1990, ApJ, 365L, 43

Wilkinson, P.N., Browne, I.W.A., Patnaik, A.R., Wrobel, J.M., & Sorathia, B. 1998, MNRAS, 300, 790

Wisotzki, L., Wucknitz, O., Lopez, S., & Sorensen, A.N. 1998, A&A, 339L, 73

Comp	$S_{1.4}$	S_5	$S_{8.4}$	S_{15}
A	70.8 ± 0.3	55.8 ± 0.1	25.5 ± 0.1	14.8 ± 0.4
B	14.5 ± 0.3	10.8 ± 0.1	5.3 ± 0.1	3.4 ± 0.4

Table 1: VLA component flux densities (in mJy) at 1.4, 5, 8.4 and 15 GHz. Data for the 1999 July 29 observation. Errors in the flux densities are taken to be equal to the rms noise of the respective maps.

Component	$\Delta\alpha$	$\Delta\delta$	S_5 (mJy)	$S_{1.7}$ (mJy)
A1	0	0	31.0	42.7
A2	$-0''\!.0203$	$-0''\!.0037$	8.3	14.4
A3	$-0''\!.0030$	$-0''\!.0024$	0.8	9.4
B1	$+0''\!.0113$	$-1''\!.3638$	6.2	9.2
B2	$+0''\!.0188$	$-1''\!.3638$	1.9	2.8

Table 2: VLBA data for B2319+051. Positions are from the 18 September 2000 5 GHz observation, and are offset from RA 23 21 40.8015 Dec +05 27 37.2252 (J2000). Flux densities are listed for both the 5 GHz and 1.7 GHz VLBA observations. Model-fitting errors are $\simeq \pm0.1$ mas for the positions of A1, A2, B1 and B2. The positional error for A3 is substantially larger ($\simeq 1$ mas). Uncertainties on the flux densities are $\simeq 5\%$.

Component	$\Delta\alpha$	$\Delta\delta$	m_{F160W}
G1	0	0	18.2
G2a	$-2''\!.257$	$2''\!.421$	19.1
G2b	$-2''\!.957$	$1''\!.777$	

Table 3: NICMOS galaxy positions and integrated magnitudes for B2319+051. The errors on the positions are $\pm0''\!.015$. The errors on the magnitudes are ±0.15.

Parameter	Value
f_{G1}	0.63
σ_{G1}	237.7 km/s
$(x, y)_{G1}$	$(+0{.}''2085, -0{.}''7891)$
PA_{G1}	$+52°$
γ	0.141
PA_γ	$-22.4°$
$(x, y)_{src1}$	$(+0{.}''2809, -0{.}''7606)$
$(x, y)_{src2}$	$(+0{.}''2787, -0{.}''7583)$
$\mu_{A1,A2}$	$+12.73, +11.82$
$\mu_{B1,B2}$	$-2.62, -2.61$
Δt	$17.8\ h^{-1}$ days
χ^2/NDF	0.45

Table 4: The best-fit SIE + shear model parameters for B2319+051. All values assume a flat $\Omega_\Lambda = 0.7$ cosmology. Listed are the fixed surface density axial ratio f_{G1}, velocity dispersion σ_{G1}, coordinates $(x, y)_{G1}$ and fixed position angle PA_{G1} for the SIE; magnitude γ and position angle PA_γ for the external shear; recovered source coordinates $(x, y)_{src}$, predicted magnifications μ and time delay Δt. The image positions are reproduced almost exactly, and are not listed.

Fig. 1.— VLA 8.4 GHz discovery snapshot observation of B2319+051 taken 1995 August 29. The lowest contour is at $\pm 3\%$ of the map peak of 26.3 mJy/beam, and contour levels increase by factors of 2. The synthesized beam is $0\rlap{.}''276 \times 0\rlap{.}''219$ at $17.4°$. The data have been naturally weighted.
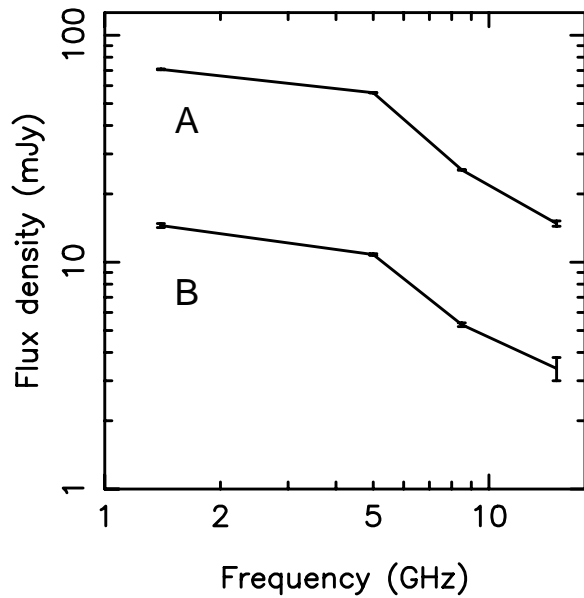

Fig. 2.— Component radio spectra based on the VLA 1.4, 5, 8.4 and 15 GHz data of 1999 July 29.
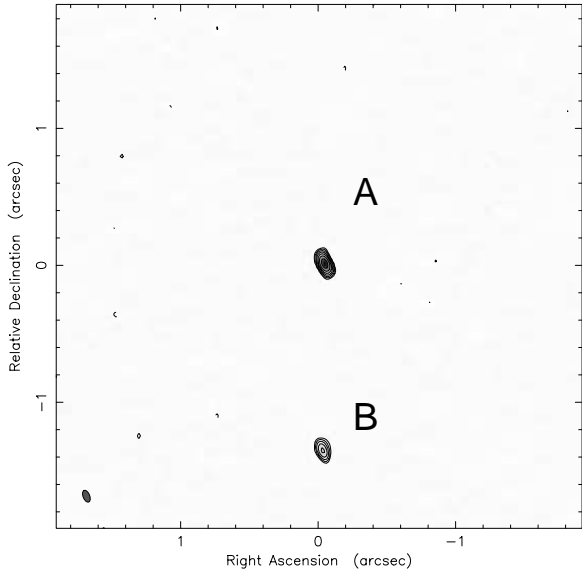
Fig. 3.— MERLIN 5 GHz observation of B2319+051 taken 1998 February 24. The lowest contour is at ±1% of the map peak of 42.4 mJy/beam, and contour levels increase by factors of 2. The synthesized beam is $0\rlap{.}''091 \times 0\rlap{.}''048$ at 21.9°. The data have been naturally weighted.
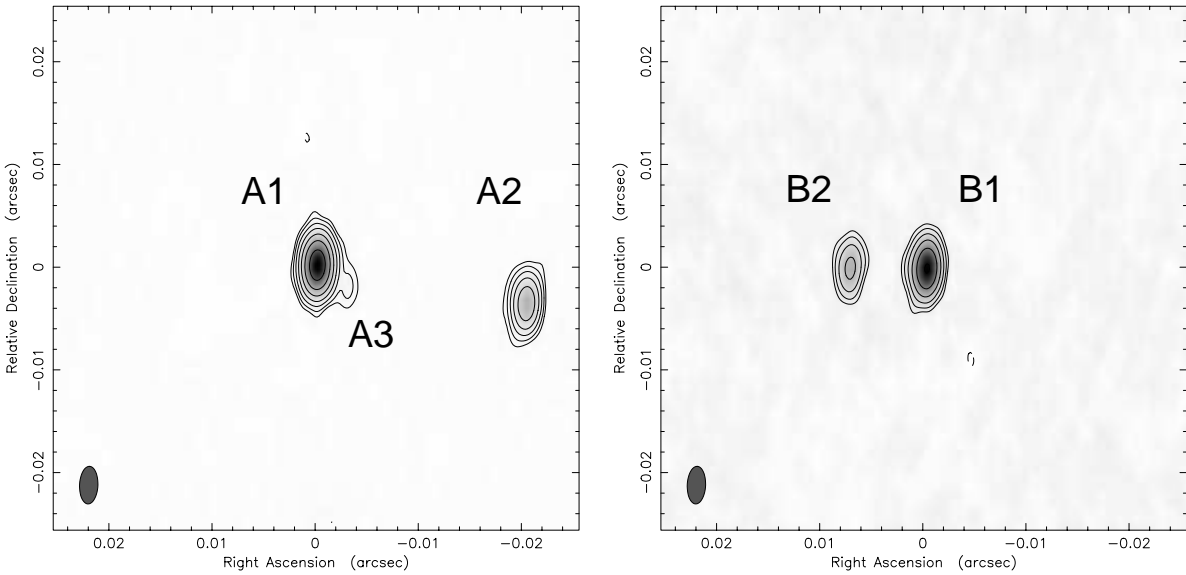

Fig. 4.— VLBA 5 GHz observation of B2319+051 taken 2000 September 18. The beam is 3.7×1.8 mas at −2.5°. The data have been naturally weighted. (a) Left: Component A. The lowest contour is at ±1% of the map peak of 30.1 mJy/beam, and contour levels increase by factors of 2. (b) Right: Component B. The lowest contour is at ±3% of the map peak of 5.9 mJy/beam, and contour levels increase by factors of 2.
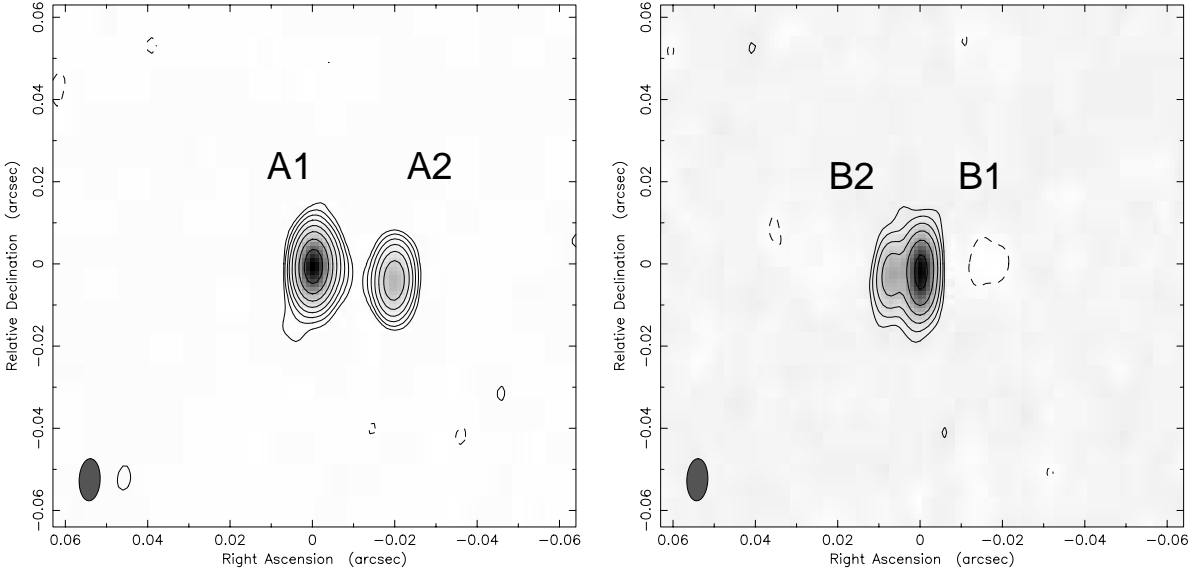
Fig. 5.— VLBA 1.7 GHz observation of B2319+051 taken 1999 August 12. The beam is 10.3×5.1 mas at $-2.6°$. The data have been naturally weighted. (a) Left: Component A. The lowest contour is at $\pm 0.5\%$ of the map peak of 46.8 mJy/beam, and contour levels increase by factors of 2. (b) Right: Component B. The lowest contour is at $\pm 2.5\%$ of the map peak of 6.3 mJy/beam, and contour levels increase by factors of 2.
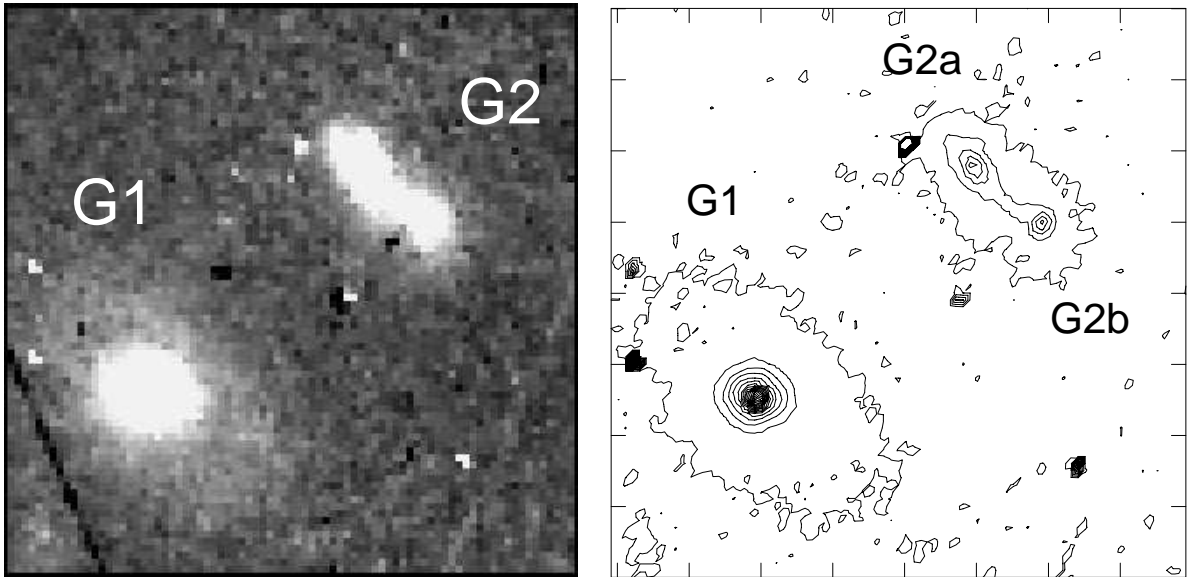

Fig. 6.— NICMOS F160W images of B2319+051. North is up, east is left. The area shown is $6\rlap{.}''0 \times 6\rlap{.}''0$. (a) Left: Final map. (b). Right: Contour map. The contour levels are $(1, 2, 3, \ldots 28)$ $\times$ rms noise in the image. Note the absence of any counterparts to the lensed radio images, and the two surface brightness peaks of G2.
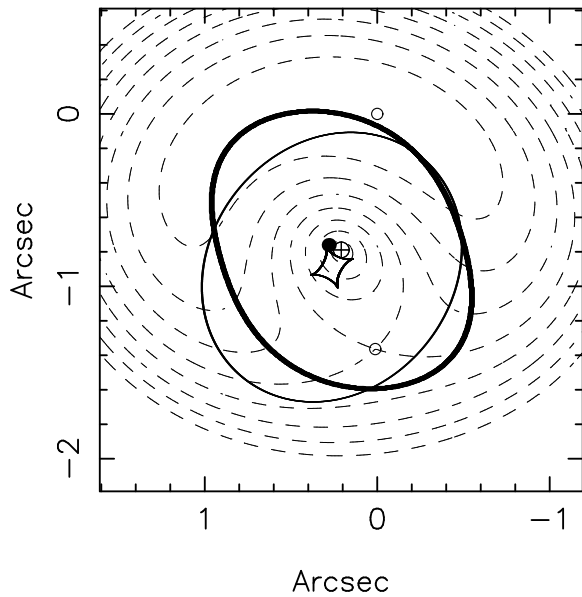
Fig. 7.— The critical curve (thick line) and caustics (thin lines) of the SIE + shear lens model. The filled circle marks the recovered source position. The open circles indicate the positions of the images. The center of the SIE is marked by the cross-haired circle. Dashed lines denote contours of constant time delay in increments of $4.45h^{-1}$ days outward from the global minimum at image A. The caustics are offset from the position of the lensing galaxy due to our choice of "centering" the shear at (0,0). This has no effect on the optimized model parameters or predicted time delay.